Int J Adv Manuf Technol (2017) 89:3419–3428
DOI 10.1007/s00170-016-9271-3

ORIGINAL ARTICLE

# Extrusion limit diagram of IN 690 super-alloy tube based on hot processing map

**Chaoyang Sun**[1] · **Yu Xiang**[1] · **Geng Liu**[2] · **Xun Zuo**[1] · **Mengqi Wang**[1] · **Qingdong Zhang**[1]

Received: 12 April 2016 / Accepted: 1 August 2016 / Published online: 20 August 2016

**Abstract** Extrusion limit diagram can be used to locate available deformation conditions for materials. The developed extrusion limit diagram of IN 690 (Inconel 690) tube was constructed through a new method by integrating analytic method, FE simulation and hot processing map. Extrusion force limit curve determined by the maximum extrusion pressure of the extruder, and temperature limit curve defined by the melting temperature of the material, which are two conventional curves for extrusion limit diagram, were obtained through FE simulations. Based on the hot processing map, high power dissipation efficiency limit curve calculated through analytical equations was firstly employed to construct the developed extrusion limit diagram. The overlap of reasonable regions bounded by these curves not only ensures smooth extrusion process, but also guarantees qualified products. Given that some special conditions were verified through FE simulations and one condition was validated through the on-site testing, the optimum region on the extrusion limit diagram is thus authentic and practical for the extrusion process of the IN 690 tube.

**Keywords** Extrusion limit diagram · Hot processing map · IN 690 super-alloy · FE simulation

## 1 Introduction

High nickel content super alloy Inconel 600 is used in high temperature corrosive environments in the nuclear industry due to its good stress corrosion cracking (SCC) resistance. Beyond that, industry has turned to improved primary water SCC (PWSCC) resistance by using high chromium content nickel-based alloys such as Inconel alloy 690 which contains ~30 wt% Cr. When the chromium content approaches 30 wt%, a protective chromium oxide layer forms, which is sufficiently dense to mitigate further corrosion in both air and steam environments [1]. Some researches mainly focused on improving the material's resistance to corrosion through changing the chemical composition [2, 3]. But Dutta [4] deemed that the best microstructure of IN 690 acquired through fully dynamic recrystallization during hot deformation can improve the resistance to corrosion in another respect.

In the past decades, hot processing maps based on the dynamic material model (DMM) [5, 6] have been employed to understand deformation mechanisms and to determine the optimal deformation parameters for practical applications. Some researchers have applied it to investigating the hot workability of IN690 super-alloy. Guo [1] constructed the hot processing map for IN 690, revealing reasonable regions for hot deformation without any further research in the application of it [5, 7]. Lv [8] studied the hot workability of IN 690 at high temperatures and strain rates based on hot processing maps, but

**Highlights** • New extrusion limit diagram integrates processing map, analytic and FE method
• Flow diagram for the integrated extrusion limit diagram is put forward
• Optimum region ensures smooth extrusion process and qualified products
• Some special conditions in the optimum region were verified
• FE model was verified through the on-site testing

✉ Chaoyang Sun
suncy@ustb.edu.cn

[1] School of Mechanical Engineering, University of Science and Technology Beijing, 30 Xueyuan Road, Haidian District, Beijing 100083, China

[2] School of Materials Science and Engineering, University of Science and Technology Beijing, Beijing 100083, China

the characteristics of different regions on the conventional processing map should be further detailed. On the hot processing map, regions for obtaining fine grain microstructures or avoiding defects during deformation can be easily located, but researches of how to use it are barely found.

Hot extrusion is the widely used processing method to manufacture IN 690 tube. But owing to the high strength, low ductility and narrow processing temperature range of the material, the defects such as tearing, surface cracking and inhomogeneous microstructure always occur during the hot extrusion. It is crucial to select reasonable thermal deformation parameters for practical industrial production, so as to obtain IN 690 super-alloy tube of fine grain microstructure and good quality. Extrusion limit diagram has been used to locate the reasonable regions for processing bars and pipes. Hirst [9] propounded the concept of extrusion limit diagram and developed the plotting method firstly. Lapovok [10], considering the effect of extrusion ratio, applied the finite element method (FEM) to constructing extrusion limit diagram for the AZ31 bar. With a brief consideration of the peak stress constitutive equation and billet size factors, Barnett [11] developed an extrusion limit diagram of the magnesium alloy bar by using analytic method. Through changing the content of Al in the magnesium alloy, Dale [12] employed the analytic method to develop an extrusion limit diagram of the magnesium alloy bar. Sun [13] constructed the extrusion limit diagram for AZ31 magnesium alloy tubes by combining FEM with analytic method. Although the commonly used extrusion limit diagram, involving extrusion force limit curve and eutectic temperature curve, can determine the region for processing acceptable extrusion products, it cannot clarify the domain for obtaining qualified products of fine grain microstructure. In addition, researches on the hot extrusion process of IN 690 super-alloy tube are rare to be seen.

In this paper, an improved extrusion limit diagram of IN 690 super-alloy tube was constructed depending on the integration of analytic method, FE simulation and hot processing map, aiming at identifying optimal region for practical industrial production. In addition, verified via FE simulations in terms of average grain size, demoulding temperature and peak extrusion force, as well as the on-site testing of one particular condition, the research is valuable and practical for production processes.

## 2 Hot workability analysis based on the processing map

Processing maps are constructed based on the dynamic material model (DMM) in which the materials are considered as a dissipater of power [14]. The dynamic power dissipation at a certain deformation condition, i.e. at a constant temperature $T$ and strain rate $\dot{\varepsilon}$, is partitioned by strain rate sensitivity ($m$). It is clear that the majority of dissipated power transformed into heat resulting in temperature rise, and only a small fraction of energy causes microstructural evolution [15]. The total power dissipation ($P$) consisting of two complementary functions $G$ and $J$ is given by:

$$P = \sigma\dot{\varepsilon} = G + J = \int_0^{\dot{\varepsilon}} \sigma d\dot{\varepsilon} + \int_0^{\sigma} \dot{\varepsilon} d\sigma \qquad (1)$$

Where $\sigma$ is the flow stress. The quantity $G$ which is given under the true stress - true strain rate curve, is designated as 'dissipater power content' and its complementary component $J$ as the 'dissipater power co-content' [16–18]. $J$ in the model is assumed to be related to the microstructural changes occurring along with the deformation, as opposed to $G$ which is related to continuum effects. Generally, most of the dissipation attributes to the temperature rise ($G$ content), while a small amount attributes to microstructural changes ($J$ content). According to the dynamic constitutive equation for a certain condition of strain, temperature and initial microstructure, the energy partitioning between $G$ and $J$ is determined by the strain rate sensitivity parameter ($m$) as follows:

$$\begin{aligned} m &= \frac{\partial \ln\sigma}{\partial \ln\dot{\varepsilon}} = \frac{\dot{\varepsilon}\,\partial\sigma_{\mathrm{DRX}}}{\sigma_{\mathrm{DRX}}\partial\dot{\varepsilon}} = \frac{\dot{\varepsilon}}{\sigma_{\mathrm{DRX}}}\frac{\partial\sigma_{\mathrm{DRX}}}{\partial X_{\mathrm{DRX}}}\frac{\partial X_{\mathrm{DRX}}}{\partial\dot{\varepsilon}} \\ &= \frac{\dot{\varepsilon}}{\sigma_{\mathrm{DRX}}}(\sigma_{\mathrm{ss}}-\sigma_{\mathrm{sat}})\frac{\mathrm{d}X_{\mathrm{DRX}}}{\mathrm{d}\dot{\varepsilon}} = \frac{\mathrm{d}J}{\mathrm{d}G} \end{aligned} \qquad (2)$$

Where $\sigma_{\mathrm{ss}}$ is the flow stress when the dislocation density $\rho$ of the material reaches the dynamic balance ($\mathrm{d}\rho/\mathrm{d}\varepsilon = 0$); $\sigma_{\mathrm{sat}}$ is the steady state stress of the experimental data; and $X_{\mathrm{DRX}}$ is the dynamic recrystallization (DRX) volume fraction.

The variation of the dimensionless parameter $\eta$, called the efficiency of power dissipation, is given by:

$$\eta = \frac{J}{J_{\max}} = \frac{2m}{m+1} \qquad (3)$$

Furthermore, the principles of irreversible thermodynamics as applied to continuum mechanics of large plastic flow are explored to define a criterion for the onset of flow instability given by the equation for the instability parameter $\xi$ which was first proposed by Ziegler based on the DMM theory [19]:

$$\xi(\dot{\varepsilon}) = \frac{\partial \ln[m/(m+1)]}{\partial \ln(\dot{\varepsilon})} + m\Big|_T \leq 0 \qquad (4)$$

Isothermal compression experiments of IN 690 super-alloy were conducted in the temperature range of 1000 °C - 1200 °C and strain rate range of 0.01–10 $s^{-1}$ with the maximum compression ratio of 55 % on the Gleeble-3500 thermal mechanical simulator. The compressed specimens were sectioned parallel to the deformation axis, mounted and then polished in hydrochloric acid water solution (copper chloride 2 g, hydrochloric acid 20 ml, water 20 ml). The true stress - true strain curves are shown in Fig. 1, and the hot processing map is plotted at the strain of 0.6 in Fig. 2.

There is one area (coloured region) in which the power dissipation efficiency is higher than 0.3: temperature range of 1125–1200 °C/ strain rate ranging from 0.1 $s^{-1}$ to 10 $s^{-1}$. High efficiency domain represents a microstructural mechanism that has dissipated the power in the most efficient way during deformation. It follows that high efficiency domain ensures optimal deformation conditions for suitable microstructural control and reproducibility [15, 20, 21].

As shown in Fig. 3, along with the increase of dissipation efficiency, the finer equiaxed crystal grains emerge.

According to the instability criterion Eq. (4), the shaded domain on the map where the newly produced entropy in the system is less than the external increased entropy is unsafe for processing. The instability area mainly appears from 1000 °C to 1140 °C in the high strain rate range and in the range of temperature lower than 1050 °C with lower strain rate. In comparison with the IN 690 super-alloy hot processing map constructed by Lv [8](1000 °C − 1250 °C)and in view of the growth of the instability area, the domain of temperature over 1220 °C can also be considered as an unstable region for processing.

## 3 Development of hot extrusion limit diagram

In order to obtain qualified metal products, extrusion process parameters, such as billet preheating temperature and extrusion speed, must be controlled effectively. Generally, extrusion limit diagram is used to describe the effects of temperature and velocity on the extrusion process. Conventional extrusion limit diagram takes extrusion force limit curve and eutectic temperature limit curve as boundaries of the region for the safe extrusion. The previous extrusion force limit diagrams were constrained because of the limited capital and time in a large amount of experiments. So a lot of new researches relating to the extrusion limit diagram were conducted based on FE simulation [8, 22, 23].

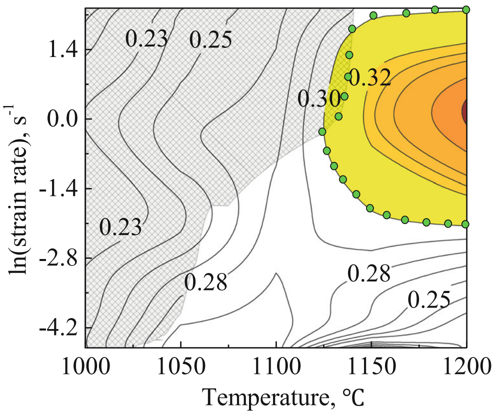

**Fig. 2** Hot processing map of IN 690 super-alloy based on Prasad criterion at the strain of 0.6 (contour numbers represent power dissipation efficiency; grey shaded area is the flow instability region; coloured area delineates the region of higher power dissipation efficiency)

### 3.1 Construction and verification of FE model

Figure 4 (a) is the schematic diagram of die structure which includes ram, die, billet, pressure pad, mandrel and container. Fig .4 (b) shows the 2D axisymmetric FE model. The values of $l_0$, $l_1$ and $l_2$ are 600 mm, 80 mm and 40 mm, respectively. $D_0$, $D_1$ are the inner and outer diameters of the tube, and $D_2$ is the diameter of the container. $D_0$ is 60 mm, $D_1$ is 80 mm, and $D_2$ is 240 mm. In the simulations, the friction coefficient is 0.08 at all contact surfaces. $\alpha$ is the semi cone angle of the 65 MN extruder. The preheating temperature of the die is 350 °C.

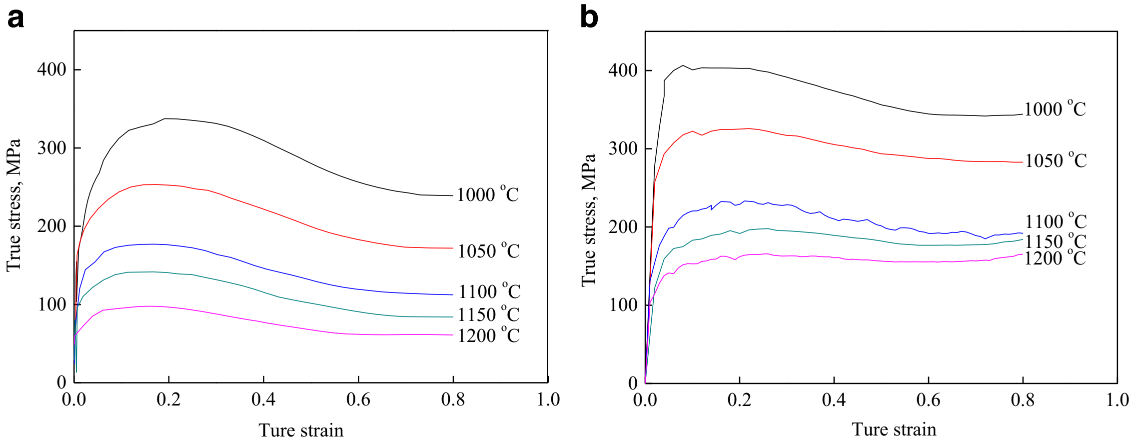

**Fig. 1** True stress - true strain curves of the experimental material obtained at strain rates: (a) 1 $s^{-1}$; (b) 10 $s^{-1}$

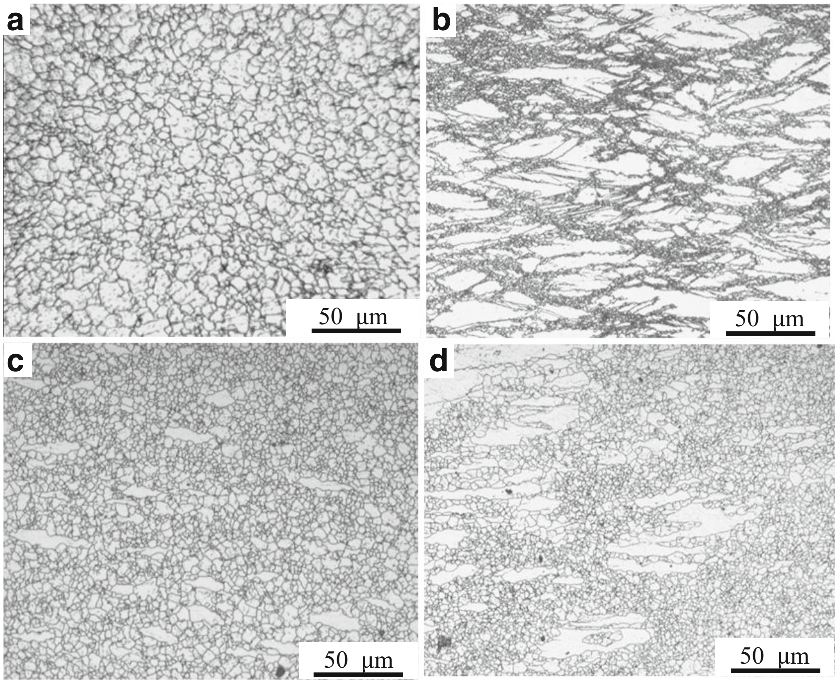

**Fig. 3** Microstructure of IN 690 super-alloy by isothermal hot compression tests under different conditions (the quenched specimens were sectioned along the symmetry vertical axis in all micrographs): (a) initial microstructure; (b) 1000 °C/1 $s^{-1}$; (c) 1150 °C/1 $s^{-1}$; (d) 1200 °C/1 $s^{-1}$

The coefficient of heat transfer is 11 N/s/mm/°C. Environmental temperature is set to be 20 °C, and the convention coefficient is 0.02 N/s/mm/°C between die and environment. The fillet radius of the die is 10 mm. The mandrel moves along with the ram during the simulations. In the simulation, the billet underwent plastic deformation, while other parts are set as rigid body. The material of the die is H13. An enhanced technique for adaptive mesh refinement (AR) was employed to solve the large deformation problem in the simulations.

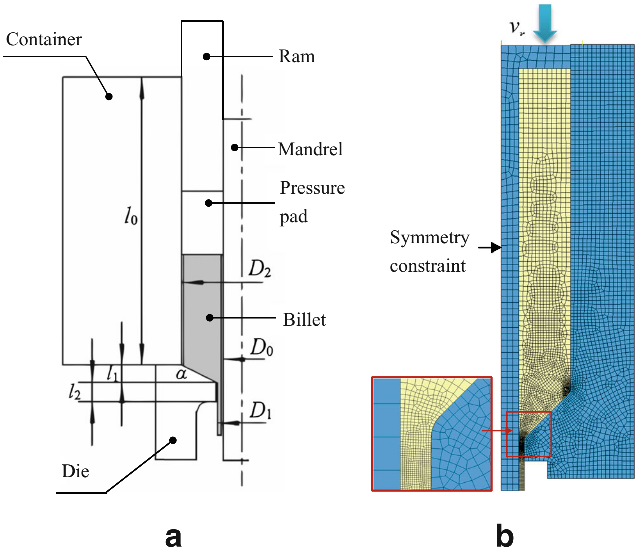

**Fig. 4** Axial-symmetrical FE model for the hot extrusion process of IN 690 alloy tube: (a) Schematic diagram of the die structure; (b) FE model

For FEM modelling, constitutive equations generated from the experimental data are given by [22, 24, 25]:

$$\sigma = \frac{1}{\alpha}\operatorname{arcsinh}\left[\exp\left(\frac{\ln\varepsilon - \ln A + Q/RT}{n}\right)\right] \tag{5}$$

$$\begin{cases} Q = 419500 + 1995300\varepsilon - 9603500\varepsilon^2 + 16718800\varepsilon^3 - 8484000\varepsilon^4 \\ \ln A = 34.2 + 181.5\,\varepsilon - 834.5\,\varepsilon^2 + 1403.9\,\varepsilon^3 - 689.5\,\varepsilon^4 \\ n = 10.6 - 42.6\,\varepsilon + 104.4\,\varepsilon^2 - 233.9\,\varepsilon^3 + 159.2\,\varepsilon^4 \\ a = 0.008 - 0.043\,\varepsilon + 0.197\,\varepsilon^2 - 0.369\,\varepsilon^3 + 0.252\,\varepsilon^4 \end{cases} \tag{6}$$

where $Q$, $A$, $\alpha$, and $n$ are material parameters; $\varepsilon$ is the strain; and $R$ is the universal gas constant (8.314 J·mol$^{-1}$ ·°C $^{-1}$).

Fig.5 shows the comparison of the experimental data and simulation data, in which the simulation result corresponds well to the experimental curve. The extrusion process can be divided into 2 stages: the filling stage and the stable stage. In the filling stage, the billet fills the cavity and the extrusion force soars because of the increase of the contact area. After the material gets through the die orifice, the extrusion force plummets and finally gets into the stable stage. The simulation curve reaches the peak firstly and it is higher than that of the experimental data (seen in regime I). The extrusion force from the experimental data is lower than the extrusion force simulated; but as increasing the deformation degree, the experimental extrusion force increases and surpasses the simulation curve (seen in regime II). This is because the lubricant becomes thinner with the increasing deformation degree in the on-site testing [26, 27]. This behaviour is not considered in FE

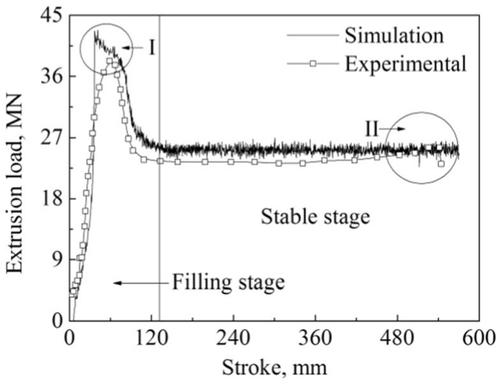

**Fig. 5** Comparison of the experimental data and simulation data at 1150 °C with extrusion speed 100 mm/s

simulations, and constant friction conditions are used. The lubricant for the on-site testing is glass powder.

### 3.2 Extrusion force limit curve

For the practical production, both mechanical properties and surface quality of the final product depend on billet temperature and extrusion speed. The rated load of the extruder used in the on-site testing is 65 MN, which is considered as the extrusion force limit. If the peak extrusion force exceeds the rated load, it may cause detrimental effects on the equipment and defects on the products.

The extrusion force limit curve is obtained through fitting the data obtained from FE simulations considering the preheating temperature and extrusion speed. As shown in Fig. 6, the extrusion force limit curve separates the diagram into two parts: the part with higher billet preheating temperature, the green shaded domain, is the safe extrusion area; while the part with lower billet preheating temperature, the orange shaded domain, is the overload area. If the billet preheating temperatures are chosen from the overload region, due to high deformation resistance, the extrusion die may be stalled, causing other accidents.

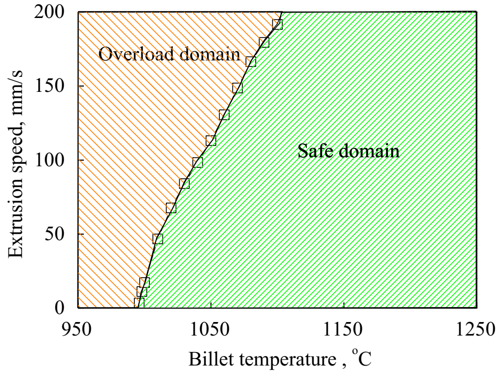

**Fig. 6** Extrusion force limit curve (orange shaded area represents the overload region; green shaded area is the region for safe extrusion)

### 3.3 Eutectic temperature limit curve

During hot extrusion processes, a large amount of heat generates due to severe plastic deformation, leading to the increase in material temperature. Whereas the IN 690 super-alloy's melting temperature is 1340 °C, the temperature limit is set as 1270 °C. If the temperature exceeds this limit, the defects, including the over-burning and surface cracking, will appear. Due to friction resistance between each part of the system and deformation of the billet, the rise in temperature is so remarkable, and it is feasible to obtain the demoulding temperature through FE simulation. Table 1 is the quantitative data of eutectic temperature limit curve, and the fraction of the deformation energy converted into heat is set to be 90 % [13, 26–28].

As shown in Fig. 7, the eutectic temperature limit curve also separates the diagram into two parts: the green shaded domain of lower preheating temperature is the feasible region for extruding product that the outlet temperature does not exceeds the limit; while the black shaded domain of higher preheating temperature is the region emerging defects where the demoulding temperature exceeds 1270 °C. If the billet preheating temperature is higher than 1230 °C, the temperature of the material will rapidly exceed the temperature limit because of the heat generated in plastic deformation and by friction. With the increase of preheating temperature, allowable extrusion speed has to be decreased to keep the temperature below the high-temperature incipient melting limit.

Fig. **8** (a) shows the temperature rise simulated at the condition of initial temperature 1195 °C with extrusion speed 148 mm/s at condition A in Fig.7, in which the temperature peak is at the inner surface. Fig.8 (b) shows the extruded product at 1225 °C with extrusion speed 100 mm/s at condition B, and there is a general surface defect like the fish scale at the inner surface. Fig.8 (c) is the extruded product at

**Table 1** The quantitative data of eutectic temperature limit curve

| No. | Initial temperature, °C | Extrusion speed, mm/s | Peak temperature, °C |
|---|---|---|---|
| 1 | 1185 | 227 | 1279 |
| 2 | 1190 | 191 | 1271 |
| 3 | 1195 | 148 | 1274 |
| 4 | 1200 | 120 | 1271 |
| 5 | 1205 | 92 | 1277 |
| 6 | 1210 | 71 | 1272 |
| 7 | 1215 | 57 | 1271 |
| 8 | 1220 | 45 | 1275 |
| 9 | 1225 | 33 | 1277 |
| 10 | 1230 | 20 | 1273 |
| 11 | 1235 | 8 | 1276 |

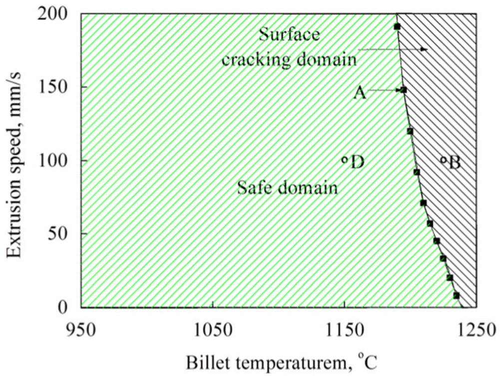

**Fig. 7** Eutectic temperature limit curve (black area represents the region causing defects on the products; green shaded area is the region for safe extrusion)

1150 °C with extrusion speed 100 mm/s at condition D, which shows the surface of the extruded product has no defect.

In the light of the analysis above, the two extrusion limit curves for conventional extrusion limit diagram have been obtained, shown in Fig.9. The conventional extrusion limit diagram only takes the rated extrusion force of the extruder and the eutectic temperature of the material as two principles for obtaining feasible parameters for practical extrusion process without considering microstructural evolution during extrusion process, which may not ensure the optimal extrusion conditions for obtaining products with fine grain microstructure.

### 3.4 High power dissipation efficiency limit curve

For the sake of applying the hot processing map to gaining products of eligible microstructure, it is necessary and feasible to use Eq. 7 to convert deformation conditions on the boundaries of unstable region and high power efficiency region into different curves on the updated extrusion limit diagram. And the validity of the equation has been verified in Sun's researches [13, 28].

$$\dot{\varepsilon} = \frac{\ln(\lambda)v_r(A_t - A_z)}{0.4\left[\left(D_2^2 - 0.75D_1^2\right)^{\frac{3}{2}} - 0.5\left(D_2^3 - 0.75D_1^3\right)\right]} \tag{7}$$

Where $\lambda$ is the extrusion ratio; $v_r$ is the extrusion speed; $A_t$ is the sectional area of the container; $A_z$ is the sectional area of the mandrel.

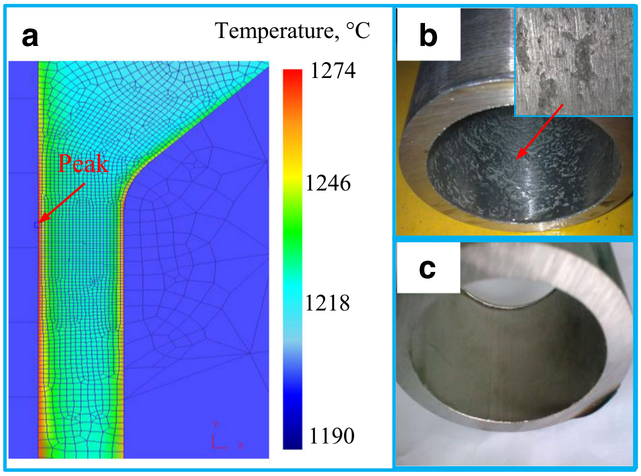

**Fig. 8** (a) Temperature of the extruded product at 1195 °C with extrusion speed 148 mm/s; (b) extruded product at 1225 °C with extrusion speed 100 mm/s at the condition B; and (c) extruded product at 1150 °C with extrusion speed 100 mm/s at the condition D

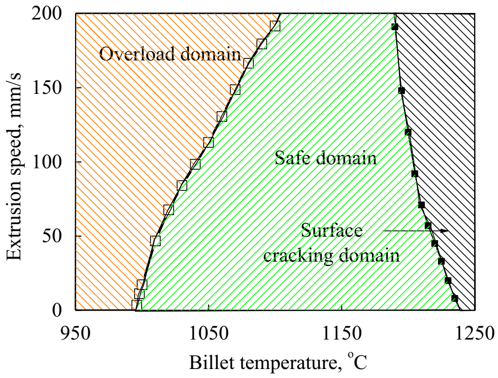

**Fig. 9** Conventional extrusion limit diagram (black area represents the region causing defects on the products; orange shaded area represents the overload region and green shaded area is the region for safe extrusion)

**Table 2** The boundary of high power dissipation efficiency region $\eta$=0.3

| No. | Temperature, °C | ln(strain rate) | Extrusion speed, mm/s |
|---|---|---|---|
| 1 | 1200.00 | 2.21 | 157.32 |
| 2 | 1182.85 | 2.25 | 163.74 |
| 3 | 1168.81 | 2.16 | 149.64 |
| 4 | 1150.77 | 2.11 | 142.35 |
| 5 | 1139.91 | 1.84 | 108.66 |
| 6 | 1138.51 | 1.30 | 63.32 |
| 7 | 1137.82 | 0.86 | 40.78 |
| 8 | 1136.02 | 0.45 | 27.06 |
| 9 | 1132.53 | 0.06 | 18.32 |
| 10 | 1124.96 | -0.24 | 13.57 |
| 11 | 1126.75 | -0.61 | 9.37 |
| 12 | 1130.44 | -0.92 | 6.87 |
| 13 | 1135.02 | -1.22 | 5.09 |
| 14 | 1141.70 | -1.51 | 3.81 |
| 15 | 1149.07 | -1.80 | 2.85 |
| 16 | 1158.05 | -1.93 | 2.50 |
| 17 | 1167.91 | -2.01 | 2.31 |
| 18 | 1178.98 | -2.08 | 2.15 |
| 19 | 1190.73 | -2.10 | 2.11 |
| 20 | 1200.00 | -2.11 | 2.09 |

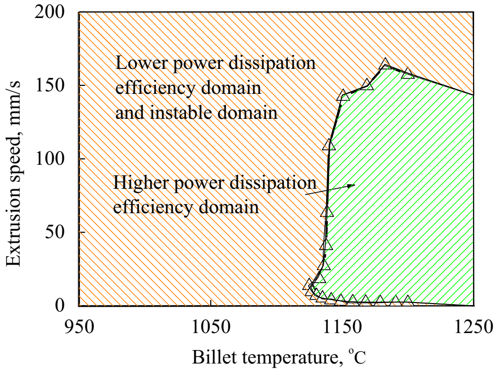

**Fig. 10** High power dissipation efficiency limit curve (orange region represents lower power dissipation efficiency region and unstable region; green shaded area represents higher power dissipation efficiency region ($\eta > 0.30$))

$$\lambda = \frac{D_2^2 - D_0^2}{D_1^2 - D_0^2} \tag{8}$$

$$A_t = \frac{\pi D_2^2}{4} \tag{9}$$

$$A_z = \frac{\pi D_0^2}{4} \tag{10}$$

On the hot processing map (Fig. 2), a series of noticeable green points around high power dissipation region ($\eta > 0.30$) are listed in Table. 2. The region bounded by these points is suitable for hot processing, in which dynamic recrystallization occurs and finer grain microstructure can be obtained (Fig. 3 (c) and (d)).

According to the Eq. 7–10, these points (green points) can be expressed against velocity and billet preheating temperature on the extrusion limit diagram (Fig. 10).

### 3.5 Optimized hot extrusion limit diagram for tube extrusion

More parameters, based on the hot processing map of IN 690 super-alloy, have been involved into the traditional extrusion limit diagram to locate the optimal region for hot extrusion process, in order to get qualified products. Figure 11 illustrates the procedure to construct the optimized extrusion limit diagram, which has been detailed in previous chapters. Through FE simulations, the two curves, extrusion force limit curve and eutectic temperature limit curve, can be obtained, which can determine the feasible region for processing on the conventional extrusion limit diagram while the excellent microstructure can not be ensured. With analytical equations, the boundary of optimal region, which is the overlap of high power efficiency domain and unstable domain on the hot processing map, can be converted into the high power dissipation efficiency limit curve on the extrusion limit diagram. A superposition of reasonable regions determines the optimized region on the new hot extrusion limit diagram, which can ensure the fine grain microstructure of final products.

The optimized extrusion limit diagram, shown in Fig.12, contains four domains: black area is the region that some

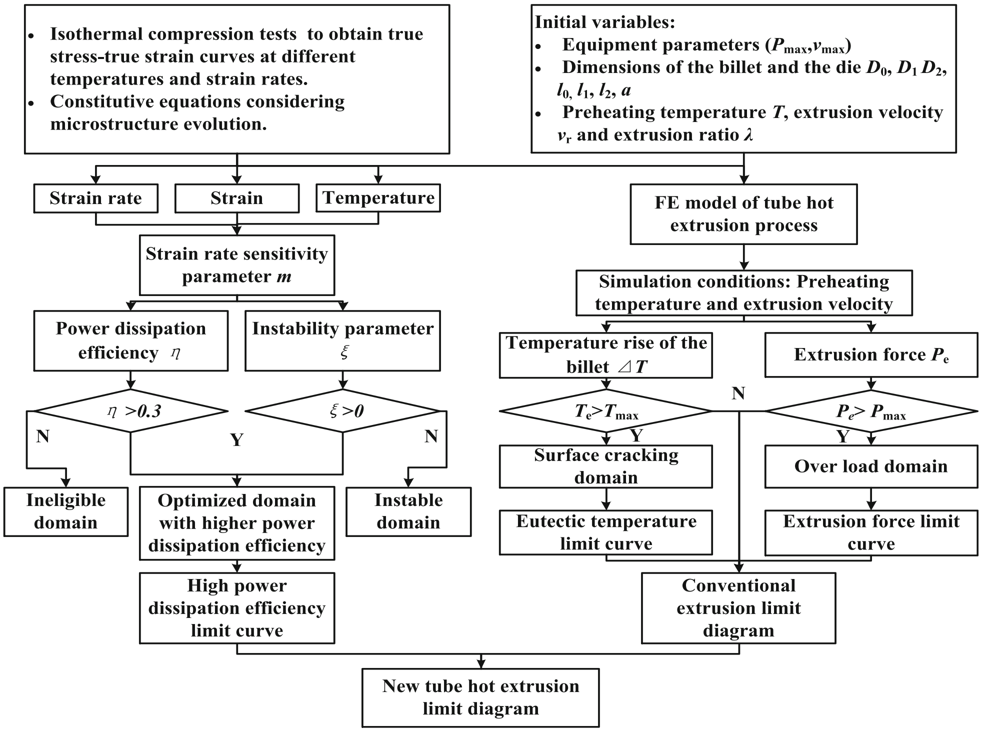

**Fig. 11** The flow diagram of constructing the optimized extrusion limit diagram

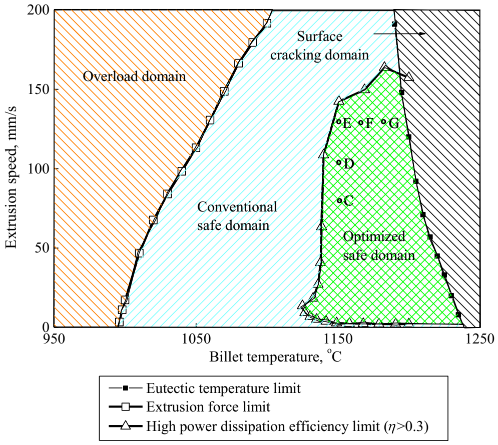

**Fig. 12** A superposition of reasonable regions (green area is available for obtaining products with excellent microstructure; orange area is the overload region; cyan area is considered as the safe domain on the conventional extrusion limit diagram; black area is the domain causing surface defects)

defects will occur; cyan area is considered as the safe region for deformation on the conventional extrusion limit diagram; orange area is the overload region that extrusion force will exceed the rated load (65 MN); and the optimal region (green shaded region) determined by different curves on the extrusion limit diagram, corresponding to the region of higher power dissipation efficiency ($\eta > 0.30$), ascertains appropriate parameters for processing qualified products. In the optimized region, the hot deformation at higher temperature with high extrusion speed is so violent that it causes increases in energy storage, the flow stress and nucleation. Therefore, the discontinuous grain growth is supressed and finer grains are obtained during high-speed extrusion (Fig. 3 (c) and (d)) [8, 21]. On the contrary, processing with large strain and lower strain rate at relatively higher temperature during the deformation, the dislocations in the alloy have enough time to slip and climb, inducing sufficient annihilation and rearrangement of grains, and the recrystallized grains have time for nucleation growth [29, 30].

## 4 Validation of the new extrusion limit diagram

Since IN 690 super-alloy is a material of low stacking fault energy, its main mechanism for grain refinement and flow softening during hot deformation process is DRX and grain growth. According to the Eq. (2), dynamic recrystallization volume fraction is introduced to reveal the variation of power dissipation during extrusion process, which indicates the keen relationship between macroscopic deformation and microstructural evolution. In order to verify the applicability of the developed extrusion limit diagram, it is necessary to conduct metallographic observation of the extruded product [8, 21, 31].

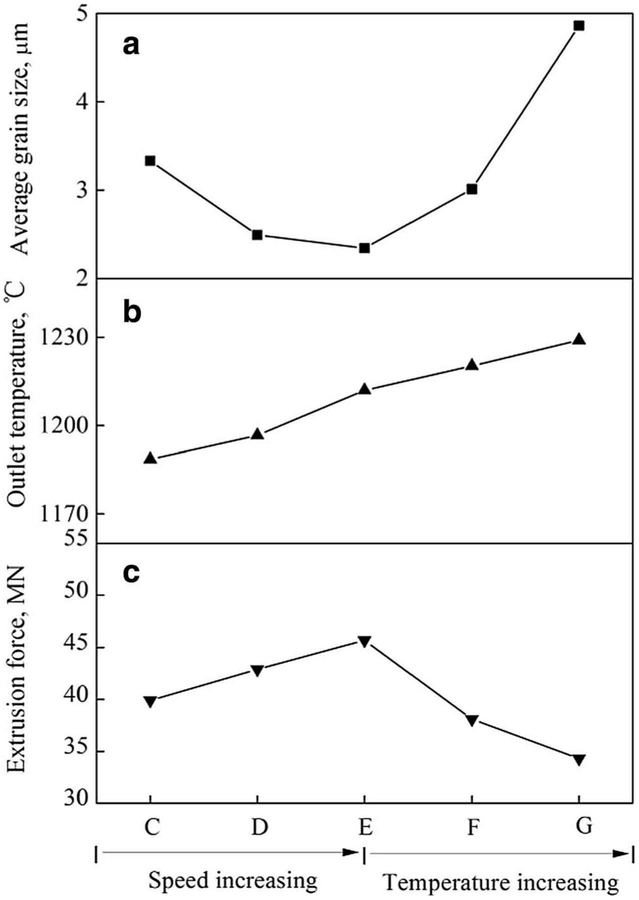

**Fig. 13** The variations of: (a) the average grain size; (b) outlet temperature; and (c) the peak extrusion force

FE simulation for microstructural evolution has been performed by using commercial FE package. Through the regression analysis of experimental data obtained in the isothermal compression tests, the microstructural evolution models constructed for IN 690 super-alloy were verified in the references [24, 25], including functions of dynamic recrystallization and grain growth. The dimensions of each part in the simulations are same to the dimensions as stated above in Fig. 4, and the parameters in the simulations (i.e., frictions) are also same to these during the simulations for constructing the extrusion limit diagram. Adaptive mesh refinement (AR) was employed for large deformation simulations under five conditions shown in Fig. 13 and in Table 3. The initial grain size of the billet in these simulations is as same as the experimental value $d_0 = 30\ \mu\text{m}$.

**Table 3** Conditions for simulation

| Extrusion condition | C | D | E | F | G |
|---|---|---|---|---|---|
| Billet temperature (°C) | 1150 | 1150 | 1150 | 1165 | 1180 |
| Extrusion speed (mm/s) | 75 | 100 | 125 | 125 | 125 |

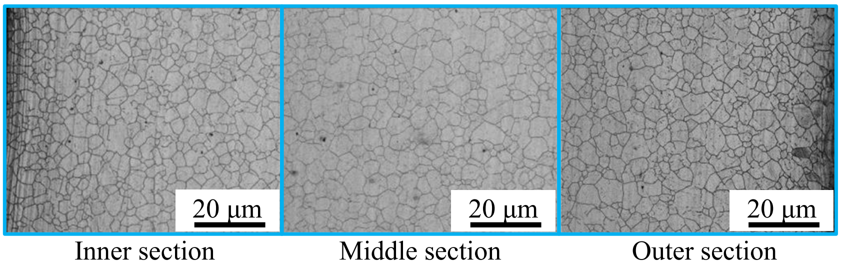

**Fig. 14** Microstructure of IN 690 super-alloy tube at condition D

By tracing centre point of grains, the parameters, such as average grain size, outlet temperature and the extrusion force are shown in Fig. 13, separately. With the rise of ram speed, strain rate increases and average grain size decreases, while outlet temperature and peak extrusion force soar due to violent deformation. On the other hand, grain growth and slight increase of temperature during extrusion process can cause decrease in peak extrusion force.

Fig.14 shows the microstructure of IN 690 super-alloy pipe extruded at condition D, which corresponds well to the simulation result in Fig.13 (a).

## 5 Conclusions

By integrating analytic method, FE simulation and hot processing map, an approach to determining the extrusion limit for IN690 super-alloy tube is presented and verified. The following conclusions are drawn:

1) A new method for constructing the extrusion limit diagram, by integrating hot processing map, analytic method and FE simulation, was firstly proposed. A flow diagram was given to illustrate the process for constructing a new tube hot extrusion limit diagram. Three main curves, including extrusion force limit curve, eutectic temperature limit curve and high power dissipation efficiency limit curve, were obtained to construct the optimized tube hot extrusion limit diagram.
2) FE model for simulations was verified through on-site testing in two aspects including the extrusion force of macroscopic deformation and microstructure examination. Some special conditions in the predicted optimal region were verified through FE simulations in the present work in terms of grain size, extrusion force and outlet temperature of the product.
3) During extrusion process with parameters chosen in the optimized region on the developed extrusion limit diagram, not only safe extrusion process but also quality and fine grain microstructure of final products can be guaranteed.

**Acknowledgments** The work presented in this paper has been supported by National Science and Technology Major Projects 'High-end CNC Machine Tools and Basic Manufacturing Equipment' (No.2014ZX04014-51), National Natural Science Foundation of China (No. 50831008, 51105029, 51575039) and NSAF (No. U1330121).

## References

1. Guo SL, Li DF (2011) Hot deformation and processing maps of Inconel 690 superalloy. J Nucl Mater 410:52–58
2. Jeng SL, Lee HT, Rehbach WP, Kuo TY, Weirich TE, Mayer JP (2005) Effects of Nb on the microstructure and corrosive property in the alloy 690-SUS 304 L weldment. Mater Sci Eng A 397:229–238
3. Li H, Xia S, Liu W (2012) C-Cr segregation at grain boundary before the carbide nucleation in alloy 690. Mater Charact 66:68–74
4. Dutta RS (2005) Corrosion aspects of Ni-Cr-Fe based and Ni-Cu based steam generator tube materials. J Nucl Mater 393:343–349
5. Prasad YVRK, Rao KP (2009) Effect of homogenization on the hot deformation behaviour of cast AZ31 magnesium alloy. Mater Des 30:3723–3730
6. Babu KA, Mandal S, Kumar A, Athreya CN, Sarma VS (2016) Characterization of hot deformation behavior of alloy 617 through kinetic analysis, dynamic material modeling and microstructural studies. Mater Sci Eng A 664:177–187
7. Suresh K, Rao KP, Prasad YVRK (2014) Study of hot forging behavior of as-cast Mg-3Al-1Zn-2Ca alloy towards optimization of its hot workability. Mater Des 57:697–704
8. Lv YC, Ren YL (2009) The study on the hot extrusion working parameters of Inconel 690 based on processing maps. Journal of plasticity engineering 12:39–44
9. Hirst (1958) Extrusion limits of magnesium alloys. Metal Treatm Drop Forg 10:409–413
10. Lapovok RY (2004) Construction of extrusion limit diagram for AZ31 magnesium alloy by FE simulation. J Mater Process Tech 146:408–414
11. Davies C, Barnett M (2004) Expanding the extrusion limits of wrought magnesium alloys. JOM 5:22–24
12. Dale LA, Barnett MR (2007) Extrusion limits of magnesium alloys. Metall Mater Trans A 38:3032–3041
13. Sun CY, Liu G, Zhang QD (2012) Extrusion limitation for AZ31 Mg alloy tubes based on numerical simulation. Steel Res Int. Special edition:871–874
14. Prasad YVRK, Gegel HL, Doraivelu SM, Malas JC, Morgan JT, Lark KA (1984) Modeling of dynamic material behavior in hot deformation: forging of Ti-6242. Metall Mater Trans A 15:1883–1892
15. Rao KP, Prasad YVRK, Suresh K (2011) Materials modelling and simulation of isothermal forging of rolled AZ31B magnesium alloy: anisotropy of flow. Mater Des 32:2545–2553
16. Suresh K, Rao KP, Prasad YVRK, Hort N, Kainer KU (2013) Effect of calcium addition on the hot working behavior of as-cast AZ31 magnesium alloy. Mater Sci Eng A 588:272–279

17. Dharmendra C, Rao KP, Zhao F, Prasad YVRK, Hort N, Kainer KU (2014) Effect of silicon content on hot working, processing maps, and microstructural evolution of cast TX32-0.4Al magnesium alloy. Mater Sci Eng A 606:11–23
18. Prasad YVRK, Rao KP (2015) Hot working guide: a compendium of processing maps. ASM International, Cleveland USA
19. Ziegler H (1962) Some extremum principles in irreversible thermodynamics, with application to continuum mechanics. Swiss Federal Institute of Technology
20. Cavaliere P, Cerri E, Leo P (2004) Hot deformation and processing maps of a particulate reinforced 2618/Al2O3/20p metal matrix composite. Compos Sci Technol 64:1287–1291
21. Rao KP, Zhong T, Prasad YVRK, Suresh K, Gupta M (2015) Hot working mechanisms in DMD-processed versus cast AZ31-1 wt% Ca alloy. Mater Sci Eng A 644:184–193
22. Sun CY, Liu JR, Li R (2011) Constitutive relationship of IN 690 superalloy by using uniaxial compression tests. Rare Metals 30:81–86
23. Sun CY, Liu G, Li R (2014) Determination of hot deformation behaviour and processing maps of IN 028 alloy using isothermal hot compression test. Mater Sci Eng A 595:92–98
24. Jiang H, Yang L, Dong JX, Zhang M, Yao Z (2016) The recrystallization model and microstructure prediction of alloy 690 during hot deformation. Mater Des 104:162–173
25. Dong JX (2014) Extrusion process and microstructure controlling of nickel alloys. Metallurgical industry press, Beijing China
26. Hansson S, Jansson T (2010) Sensitivity analysis of a finite element model for the simulation of stainless steel tube extrusion. J Mater Process Tech 210:1386–1396
27. Hansson S, Fisk M (2010) Simulations and measurements of combined induction heating and extrusion processes. Finite Elem Anal Des 46:905–915
28. Sun CY, Liu D, Fu MW (2016) Investigation of extrusion limit of Incoloy028 alloy tube by combining numerical and analytical methods. Int J Adv Manuf Technol 83:177–185
29. Wang S, Hou LG, Luo JR (2015) Characterization of hot workability in AA7050 aluminium alloy using activation energy and 3-D processing map. J Mater Process Tech 225:110–121
30. Zhang W, Liu Y, Li HZ, Li Z (2009) Constitutive modeling and processing map for elevated temperature flow behaviors of a powder metallurgy titanium aluminide alloy. J Mater Process Tech 209: 5363–5370
31. Dang L, Yang H, Guo LG, Zeng WD (2015) Study on exit temperature evolution during extrusion for large-scale thick-walled Inconel 625 pipe by FE simulation. Int J Adv Manuf Technol 76: 1421–1435